Chapter 7

Examination of Mechanical Properties of Human Vertebral Cancellous Bone Using Combined Unit Cell Models

7.0 Abstract

A three-dimensional structural model composed of two different unit cells, which have distinct mechanical behavior in the vertical direction, with doubly tapered struts for human vertebral cancellous bone is proposed in this chapter. The ensemble-volume and orientation averaging procedures are employed to derive the equations. The effects of age-related changes in vertebral cancellous bone on effective stiffness and collapse stress in both horizontal and vertical directions are studied. The predicted mechanical behaviors of human vertebral cancellous bone are generally consistent with experimental observations in literature.

7.1 Introduction

Fractures resulting from minimal trauma can result in significant morbidity and mortality in the elderly. These fragility fractures are related to underlying osteoporosis, which is the most common type of bone disease. In the USA, 1.5 million osteoporosis-related fractures occur annually, including 700,000 vertebral fractures, 250,000 distal forearm fractures, 250,000 hip fractures and 300,000 fractures of other sites. These fractures have contributed to an estimated $5 to $10 billion in health care costs [1].

Studies suggest that the incidence of vertebral fracture has increased 2-4 fold during the past 30 years [2, 3]. Understanding the mechanical properties, the relationships between structures and the functions of cancellous bone are critical when developing strategies to prevent and treat osteoporosis-related fractures.

It is widely accepted that osteoporosis-related fractures are associated not only with the density of the cancellous bone, but also with the cancellous bone structure, which changes with age [4, 5]. Many researchers have tried to characterize the structure of the vertebral cancellous bone [6, 7] and quantify the effects associated with age [4-6, 8-12]. Structural models for the mechanical properties of cancellous bone have also been developed for capturing the predominant mechanical behaviors [13-21]. For example, Kim [20] used a regular hexagonal cellular structure model, comprised of doubly tapered struts, to obtain the horizontal Young's modulus and the horizontal collapse strength of vertebral cancellous bone. Sander et al. [21] developed a cellular solid model, composed of two idealized unit cell geometries, to investigate the fluid flow characteristics of human vertebral cancellous bone.

Micro-finite element methods have also been used to determine the elastic properties, local stress and failure of cancellous bone [22-29]. Compared to other structural models, the micro-finite element method can more effectively capture the real geometry of the cancellous bone, and may provide more accurate results for specific specimens under different loading conditions. However, this method requires a significant amount of computer resources, which may not be cost effective or mathematically tractable.

The purpose of this chapter is to develop a three-dimensional structural model composed of two different unit cells, which have distinct mechanical behaviors in the vertical directions for human vertebral cancellous bone. The ensemble-volume and orientation averaging procedures are employed to derive the equations. This model was used to examine the effects of age-related changes in cancellous bone on effective stiffness and maximum strength, which are then compared with experimental results.

7.2 Structural Model of Vertebral Cancellous Bone

The predominant structure of cancellous bone in the vertebra consists of vertical and horizontal plates or rods; the exact geometry depends on anatomic site, age, and health [30]. This structure can be characterized as cubic lattices of vertical columns and horizontal supporting struts with cylindrical symmetry in the central part of the vertebra; this structure is accurate for younger individuals as well [4, 16] (**Figure 7-1**). The two idealized unit cells, rectangular and offset rectangular with doubly tapered strut shapes (**Figure 7-2**), are used here to develop the model.

7.2.1 Strut Morphology and Material Properties

Mosekilde [4, 5] studied the age-related behavior of human vertebral cancellous bone structure, describing it in terms of both horizontal and vertical trabeculae mean thicknesses as well as the distances between them (**Table 7-1**). These parameters were used to determine the structure of both unit cells as a function of age.

In our model, we assume that the diameter functions of horizontal and vertical struts are

$$D(x_i) = D_{0i}\left[1 + a_i\left(\frac{x_i}{L_{ei}}\right)^2\right]^{\frac{1}{2}}, \quad i = 1,2 \tag{7.1}$$

where D_{0i} are diameter values at the mid-span ($x_i = 0$), a_i are shape parameters and L_{ei} are the half strut lengths of horizontal and vertical struts. These functions are continuous at the mid-span ($x_i = 0$) which is considered to be more realistic for the trabeculae [20]. In Eq. (7.1), D_{0i} can be obtained from Eq. (7.2) assuming that the tapered struts have the same volume as the uniform ones.

$$D_{0i} = \frac{\sqrt{3}}{\sqrt{3 + a_i}} D_i, \; i = 1,2 \tag{7.2}$$

From Eq. (7.1), the cross-sectional area $A(x_i)$, the second moment of area $I(x_i)$ and the plastic section modulus $Z(x_i)$ for the cross-section of the horizontal and vertical struts can be derived as

$$A(x_i) = \frac{\pi}{4} D^2(x_i) = \frac{\pi}{4} D_{0i}^2\left[1 + a_i\left(\frac{x_i}{L_{ei}}\right)^2\right], \; i = 1,2 \tag{7.3}$$

$$I(x_i) = \frac{\pi}{64} D^4(x_i) = \frac{\pi}{64} D_{0i}^4\left[1 + a_i\left(\frac{x_i}{L_{ei}}\right)^2\right]^2, \; i = 1,2 \tag{7.4}$$

$$Z(x_i) = \frac{\pi}{4} D^2(x_i) \cdot \frac{2D(x_i)}{3\pi} = \frac{1}{6} D_{0i}^3\left[1 + a\left(\frac{x_i}{L_{ei}}\right)^2\right]^{\frac{3}{2}}, \; i = 1,2 \tag{7.5}$$

The solid volume fraction, ρ^*, of each unit cell may be estimated from the following equation when the solid volume fraction is not large,

$$\rho^* \cong \frac{2\left\{2\int_0^{L_1/2} A_1(x_1)\,dx_1 + \int_0^{L_2/2} A_2(x_2)\,dx_2\right\}}{L_1^2 L_2} \tag{7.6}$$

Many researchers have tried to obtain the mechanical properties of individual trabeculae. There are several different techniques used to determine the Young's modulus of the trabeculae including direct mechanical testing of a single trabecula using direct tension tests [31, 32], buckling tests [33, 34], and bending tests [35-39]; ultrasonic approaches [32, 40]; and finite element methods [14, 17, 22-26, 28, 38, 39, 41]. The results of these tests are summarized in **Table 7-2**.

It is often reported that mechanical tests are difficult to conduct and have their associated inherent errors due to the small size of the specimens and any artifacts of the testing techniques. Consequently, direct tension and bending tests may result in a lower measured modulus than the true value [32, 42]. Gibson and Ashby [42] reviewed some of the moduli obtained by methods mentioned above and suggested a mean value of 12 GPa for the Young's modulus of the individual trabeculae; this value is assumed for the study conducted in this chapter.

There have been no reported measurements of the strength of the individual trabeculae, σ_y. Reilly and Burstein [43] and Currey [44] reported that the compressive strength of wet compact human bone is about 193 MPa. Since the constituents, compositions and elastic properties of compact and trabecular bone are nearly the same in

the bone ultrastructure [45, 46], we assume that individual trabeculae also has a compressive strength of 193 MPa.

7.2.2 Effective Stiffness of Vertebral Cancellous Bone

The effective stiffness for the rectangular and offset rectangular unit cells shown in **Figure 7-2** with horizontal struts (of length L_1) and vertical struts (of length L_2), can be determined based on the structure, mode of deflection, and material properties of the individual trabeculae (cf. **Appendix VI**).

The effective Young's modulus in the inferior-superior direction for the rectangular and offset rectangular unit cells, E_{r3}^* and E_{o3}^* respectively, are

$$E_{r3}^* = \frac{L_2}{2L_1^2 M_2} \tag{7.7}$$

$$E_{o3}^* = \frac{L_2}{L_1^2\left[N_{o1} + 2k\left(1+\nu\right)M_{o1} + 2M_2\right]} \tag{7.8}$$

where M_2, N_{o1} and M_{o1} are compliance functions of the struts as follows, ν is Poisson's ratio of the strut material and k is a shear correction coefficient, which is about $10/9$ for a circular section.

$$\begin{aligned} M_2 &= \int_0^{L_2/2} \frac{1}{EA_2\left(x_2\right)} dx_2 \\ M_{o1} &= \int_0^{L_1/4} \frac{1}{EA_1\left(x_1\right)} dx_1 \text{ and } N_{o1} = \int_0^{L_1/4} \frac{x_1^2}{EI_1\left(x_1\right)} dx_1 \end{aligned} \tag{7.9}$$

The mixture rule [21, 47] is adopted here to model the overall effective Young's modulus in the vertical direction, which can be written as

$$E_3^* = (1-\phi)E_{r3}^* + \phi E_{o3}^* \tag{7.10}$$

where ϕ is the volume fraction of offset rectangular unit cells, which can be determined based on the linear regression relationship between apparent modulus and apparent density developed by Kopperdahl and Keaveny [48]

$$E_3^* = b\rho^*\rho \tag{7.11}$$

where $b = 2100$ MPa and ρ is the tissue mass density, which is assumed to be 2.0 $\mathrm{g/cm^3}$ [49]. Combining Eq. (7.10) and (7.11),

$$\phi = \frac{E_{r3}^* - b\rho^*\rho}{E_{r3}^* - E_{o3}^*} \tag{7.12}$$

Orientation averaging procedures, with respect to x_3-axis (cf. **Appendix IX**), and an ensemble-volume averaging scheme are then performed. The results are used to obtain the overall effective stiffness of vertebral cancellous bone from which the effective Young's moduli in the horizontal direction $\langle \bar{E}_1^* \rangle$ and $\langle \bar{E}_2^* \rangle$ can be obtained.

7.2.3 Maximum Strength of Vertebral Cancellous Bone

In this section, we assume that tissue material is rigid and perfectly plastic in order to derive the uniaxial plastic collapse stress of vertebral cancellous bone. Due to the spatially periodic nature of the unit cell structure, the individual struts deform anti-symmetrically about their mid-spans [50]. Additionally, the mechanical properties for the unit cells can be approximately determined from those of cantilever beams. The critical

vertical collapse stress takes place in the offset rectangular unit cells; whereas, the critical horizontal collapse stress occurs in the soft direction of the rectangular unit cells.

Considering the stress σ_3 to be parallel to the x_3 axis will produce an axial force P_3 on the vertical strut as well as a bending moment on the horizontal strut as shown in **Figure 7-3.** Depending on which strut fails, we can distinguish failure modes into vertical strut failures or horizontal strut failures. The bending moment at the plastic hinge section of the horizontal strut is

$$M_\lambda = \frac{P_3 \lambda_{o1}}{4} \tag{7.13}$$

where λ_{o1} is the effective length after plastic collapse. The yield condition [51] is described as

$$\frac{M_\lambda}{\sigma_y Z_\lambda} + \left(\frac{\sigma_a}{\sigma_y}\right)^2 = 1 \tag{7.14}$$

where Z_λ is the plastic section modulus at the plastic hinge section of the strut, σ_y is the yield stress of the strut material and σ_a is the internal axial stress, which is zero in this case. Substituting Eq. (7.13) and $P_3 = \sigma_3 L_1^2$ into Eq. (7.14), the upper bound on plastic collapse stress in the horizontal struts can be written as

$$(\sigma_3)_1 = \frac{4 Z_\lambda}{\lambda_{o1} L_1^2} \sigma_y \tag{7.15}$$

When the maximum stress of the vertical strut exceeds the yield stress σ_y, the vertical strut yields axially. Therefore, the collapse stress in the vertical strut is

$$\left(\sigma_3\right)_2 = \frac{\pi D_{02}^2}{4L_1^2}\sigma_y \tag{7.16}$$

When Eq. (7.16) exceeds Eq. (7.15), failure occurs in the horizontal strut. Note that Eq. (7.16) is rarely reached to in compression because of buckling.

Similarly, under the stress σ_1, parallel to the x_1 direction **(Figure 7-4),** the bending moment and axial stress at the plastic hinge section of the horizontal strut are

$$M_\lambda = \frac{P_1\lambda_1 \sin\theta}{2} \tag{7.17}$$

$$\sigma_a = \frac{P_1 \cos\theta}{A_\lambda} \tag{7.18}$$

where A_λ is the cross-section area of the horizontal strut at the plastic hinge section. Substituting Eq. (7.17), (7.18) and $P_1 = \sigma_1 L_1 L_2 \sin\theta$ into Eq. (7.14),

$$\frac{\sigma_1}{\sigma_y} = \frac{2Z_\lambda}{\lambda_1 L_1 L_2 \sin^2\theta}\left[1 - \left(\frac{\sigma_a}{\sigma_y}\right)^2\right] \tag{7.19}$$

Since the contribution of the axial load to yielding is small compared with that from the bending moment under uniaxial loading [52-54], the uniaxial horizontal collapse stress can be approximated as

$$\sigma_1 = \frac{2Z_\lambda}{\lambda_1 L_1 L_2 \sin^2\theta}\sigma_y \tag{7.20}$$

The effective length after plastic collapse, λ, can be obtained by taking the derivative of the collapse stress with respect to x in order to find the value of x for which the collapse stress is a maximum. The result is written as follows

$$\lambda = 2x_\lambda = \frac{\sqrt{2}L_e}{a} \tag{7.21}$$

The corresponding plastic section modulus is

$$Z_\lambda = \frac{1}{4}\sqrt{\frac{3}{2}}D_0^3 \tag{7.22}$$

7.3 Numerical Simulations and Results

The effective stiffness, the collapse stress and the relative density for human vertebral cancellous bone can be expressed in terms of age and sex by inserting the equations listed in **Table 7-1** into Eq. (7.1) through (7.12), Eq. (7.15), Eq. (7.16) and Eq. (7.20) through (7.22). For material properties of the individual trabeculae, ignoring any age-related changes, values of E = 12 GPa and σ_y = 193 MPa were used.

Figure 7-5 shows the relationship between age and changes in volume fraction of offset unit cells. From age 40 to 80, the volume fraction of offset unit cells increases by approximately 20% in all cases, suggesting a potentially important increase in the percentage of cancellous bone that experience bending as well as an associated decrease in the percentage of cancellous bone that experience compression. The relative density, effective stiffness and collapse stress all decrease with age as shown in **Figure 7-6** through **Figure 7-15**.

Figure 7-7 and **Figure 7-8** show the relationship between age and changes in the effective Young's modulus in the vertical and horizontal directions. Kopperdahl [48] suggested that the mean modulus estimated in previous studies [4, 5], where human

vertebral bone between platens was mechanically tested, should be 4.5-13.5 times higher than the true value if end-artifacts errors were eliminated. Therefore, an amplification factor will be used in this study; a value of 6.2 was obtained by matching experimental data.

When compared with the models of Jensen et al. [17], Overaker [19] and Kim [20], the results produced by our model are in reasonably good agreement with associated experimental data. The model presented by Jenson et al. [17] was based on the rectangular uniform columnar structure, which was too stiff in both directions, and a reduced material modulus of 3.8 GPa was used. Regular hexagonal columnar structure was the basic approach used in both of the models presented by Overaker [19] and Kim [20] to predict the mechanical properties of vertebral cancellous bone. However, the hexagonal structure used was too flexible in the in-plane direction, too rigid in the out-of-plane direction, and resulted in a much smaller relative density.

The sex-related differences in the relationships between mechanical properties and age are illustrated in **Figure 7-11** through **Figure 7-15**. The relative density of male vertebral cancellous bone is nearly 18% higher than that of females at age 40 and 12% higher at age 80. The effective Young's modulus and the collapse stress in male vertebral cancellous bone are approximately 12 to 34% higher than those of females. These sex-related differences are emerged from the variations in vertebral cancellous bone structure with a higher tendency to perforation of the horizontal supporting struts in females than in males [55].

7.4 Discussion

The mechanical properties of human vertebral cancellous bone were examined using a combined cellular solid model with doubly tapered struts. In particular, we used the orientation averaging procedure to derive the effective stiffness of each unit cell. Subsequently, we employed a volume-averaging scheme to calculate the overall effective stiffness of human vertebral cancellous bone.

Tapered strut models are better at matching experimental observations of trabecular thickening near the joints and produce more accurate mechanical properties than uniform strut models. Ensemble volume and orientation averaging schemes have allowed for the combination of two or more unit cells with different mechanical behaviors to predict an overall mechanical behavior. Our study shows that not only is bending the dominant mechanical behavior in human vertebral cancellous bone, but as age increases, so does the percentage of cancellous bone that is controlled by bending.

In the current literature, there is no model to predict the vertical collapse stress; this chapter is the first attempt to do so. In addition, based on sex-related morphology information, our model can predict those sex-related differences in the mechanical properties. In current literature, other researchers don't do that.

Considering data scattering of those experimental results [56], the proposed model predictions are in reasonably good agreement with associated experimental data. However, the model does not match well in all aspects; this is likely due to several reasons. First, the structure of the model is not an exact copy of the cancellous bone specimen but rather an idealization representing the vertebral cancellous bone over a span

of years. Second, in the experimental data, the age-related increase in distance between trabeculae is partly caused by perforations of the trabeculae and subsequent removal of the whole trabeculae [17]. However, all increases in inter-trabecular distances in the model were assumed to be generated entirely from increases in the distance between existing trabeculae. Consequently, the relative density may be underestimated in the model. Third, the age-related changes of the human vertebral cancellous bone structure were being referenced to experimental data of limited size [4, 5]. More accurate and precise regressions from a larger pool of specimens would likely yield better predictions. Fourth, the experimental protocols and the specimen size may need to be taken into consideration. Depending on the specimen size, the structural element and characteristic length may change.

Our model does not contain any plate-like structures common in cancellous bone in other sites of the body. However, the proposed model could be expanded to predict the mechanical properties of cancellous bone with a more plate-like structure. The Structural Model Index (SMI) introduced by Hildebrand, T. and P. Ruegsigger [57] can be easily incorporated into our model. The SMI can be used to quantify the characteristic form of a three-dimensional structure in terms of the volume fraction of plates and rods composing the structure.

7.5 Conclusions

To investigate the effects of age-related changes in human vertebral cancellous bone on mechanical behaviors, an analytical model is proposed. This model is composed

of two idealized unit cells with doubly tapered struts and incorporates the ensemble-volume and orientation averaging procedures. The predicted mechanical behaviors of human vertebral cancellous bone are generally consistent with experimental observations in literature. This model could serve as a theoretical framework for cancellous bone and provide assistance in understanding the connection between structural changes and biomechanical competence.

Table 7-1. The age-related changes in human vertebral cancellous bone structure based on the linear regression equations developed by Mosekilde [4, 5]

Parameters	Relationships (Age in years)
Males [5]	
Horizontal trabeculae mean thickness	$D_1(\mu m) = -1.20 \times \text{Age} + 205.2$, $r = -0.72$
Vertical trabeculae mean thickness	$D_2(\mu m) = -0.494 \times \text{Age} + 239.7$, $r = -0.28$
Distance between horizontal trabeculae	$L_2(\mu m) = 10.39 \times \text{Age} + 411.7$, $r = 0.65$
Distance between vertical trabeculae	$L_1(\mu m) = 7.49 \times \text{Age} + 402.4$, $r = 0.72$
Females [5]	
Horizontal trabeculae mean thickness	$D_1(\mu m) = -0.80 \times \text{Age} + 171.9$, $r = -0.67$
Vertical trabeculae mean thickness	$D_2(\mu m) = 0.057 \times \text{Age} + 196.2$, $r = 0.035$
Distance between horizontal trabeculae	$L_2(\mu m) = 16.01 \times \text{Age} + 161.4$, $r = 0.72$
Distance between vertical trabeculae	$L_1(\mu m) = 8.89 \times \text{Age} + 332.9$, $r = 0.66$
Both [4]	
Horizontal trabeculae mean thickness	$D_1(\mu m) = -1.03 \times \text{Age} + 189$, $r = -0.71$
Vertical trabeculae mean thickness	$D_2(\mu m) = 0.14 \times \text{Age} + 208$, $r = 0.06$
Distance between horizontal trabeculae	$L_2(\mu m) = 13.74 \times \text{Age} + 288$, $r = 0.79$
Distance between vertical trabeculae	$L_1(\mu m) = 6.74 \times \text{Age} + 456$, $r = 0.75$

Table 7-2. Young's modulus of human trabeculae from various sources

Reference	Type of bone	Method	Young's modulus (GPa)
Runkle and Pugh [33]	Distal femur	Buckling	8.69 (±3.17) dry
Townsend et al. [34]	Proximal tibia	Inelastic buckling unmachined	11.38 wet
			14.13 dry
Williams and Lewis [14]	Proximal tibia	Compression test with 2D FEM	1.30
Kuhn et al. [35]	Fresh frozen tibia	3-point bending machined	3.17 (±1.50)
Mente and Lewis [38]	Dried femur, fresh tibia	Cantilever bending with 2D FEM	5.30 (±2.60)
Ashman and Rho [40]	Femur	Ultrasonic test	13.0 (±1.50)
Choi et al. [36]	Tibia	3-point bending machined	4.59 (±1.60)
Kuhn et al. [37]	Iliac crests	3-point bending machined	3.81
Mente and Lewis [39]	Dried femur, fresh tibia	Cantilever bending with 3D FEM	7.80 (±5.40)
Jensen et al. [17]	Vertebra	3D FEM	3.80[a]
Choi and Goldstein [58]	Tibia	4-point bending machined	5.35 (±1.36) wet
Rho et al. [32]	Tibia	Tension test	10.4 (±3.50) dry
		Ultrasonic test	14.8 (±1.40) wet
Van Rietbergen et al. [22]	Proximal tibia	3D Micro-FEM	2.23~10.10 (5.91)
Overaker et al. [19]	Vertebra	Idealized model	12.0 [a]
Silva and Gibson [41]	Vertebra	2D FEM	0.10 [a]
Hou et al. [23]	Vertebra	3D Micro-FEM	5.70±1.60
Ladd et al. [24]	Vertebra	3D Micro-FEM	6.60
Homminga et al. [28]	Vertebra	3D Micro-FEM	5.0
Kim and Al-Hassani [20]	Vertebra	Idealized model	12.0 [a]
Van Rietbergen et al. [59]	Femur	3D Micro-FEM	15.0 [a]
Bini et al. [60]	Femur	Tension and compression test	1.41~1.89
Sander et al. [21]	Vertebra	Idealized model	18.0
Present Study	Vertebra	Idealized model	12.0 [a]

[a] Young's modulus of trabeculae used for an idealized model

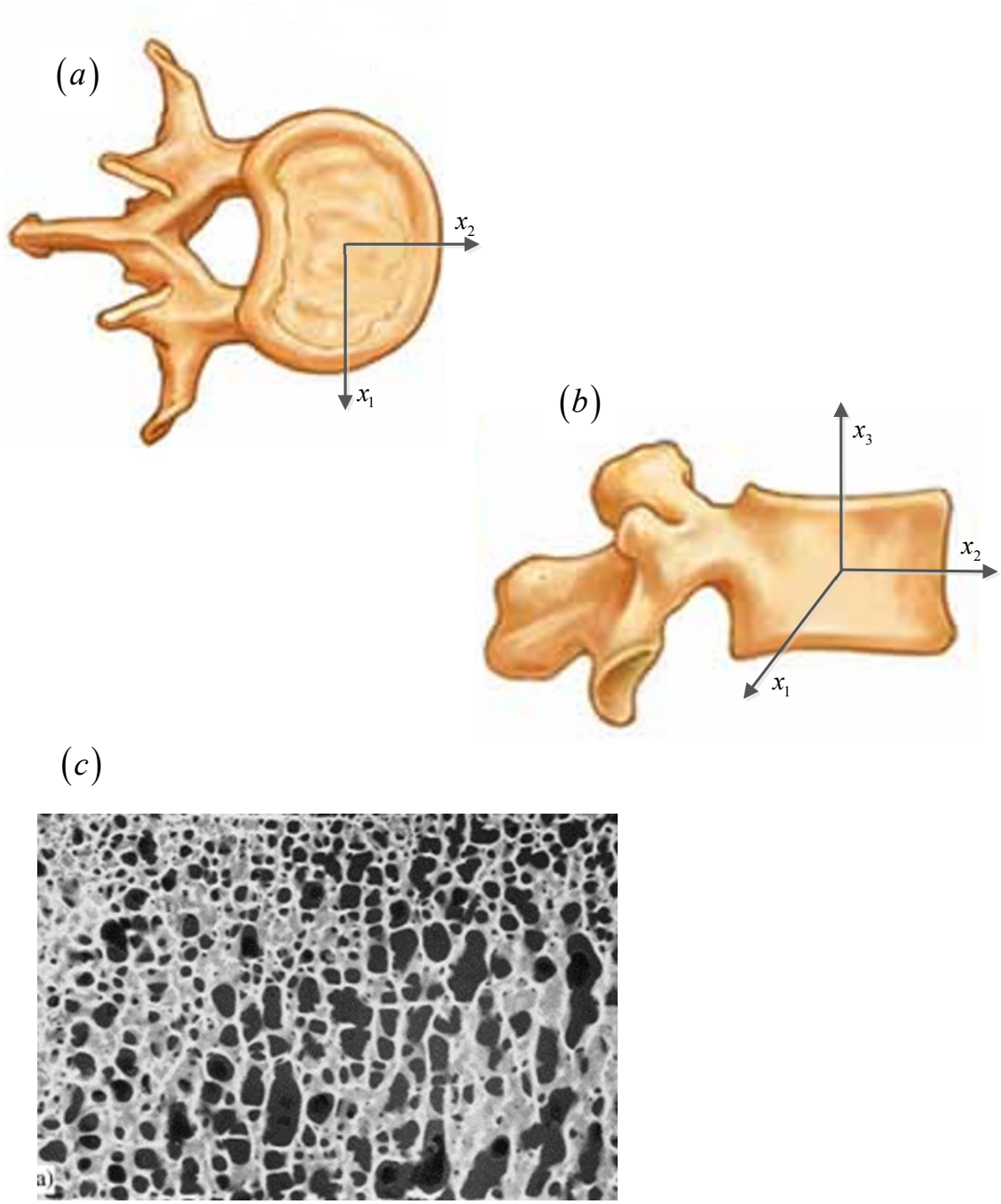

Figure 7-1. Lumbar vertebra in (a) superior and (b) lateral view. x_3 is oriented in the inferior-superior direction and is the principal loading direction. (c) A detail view of human vertebral cancellous bone.

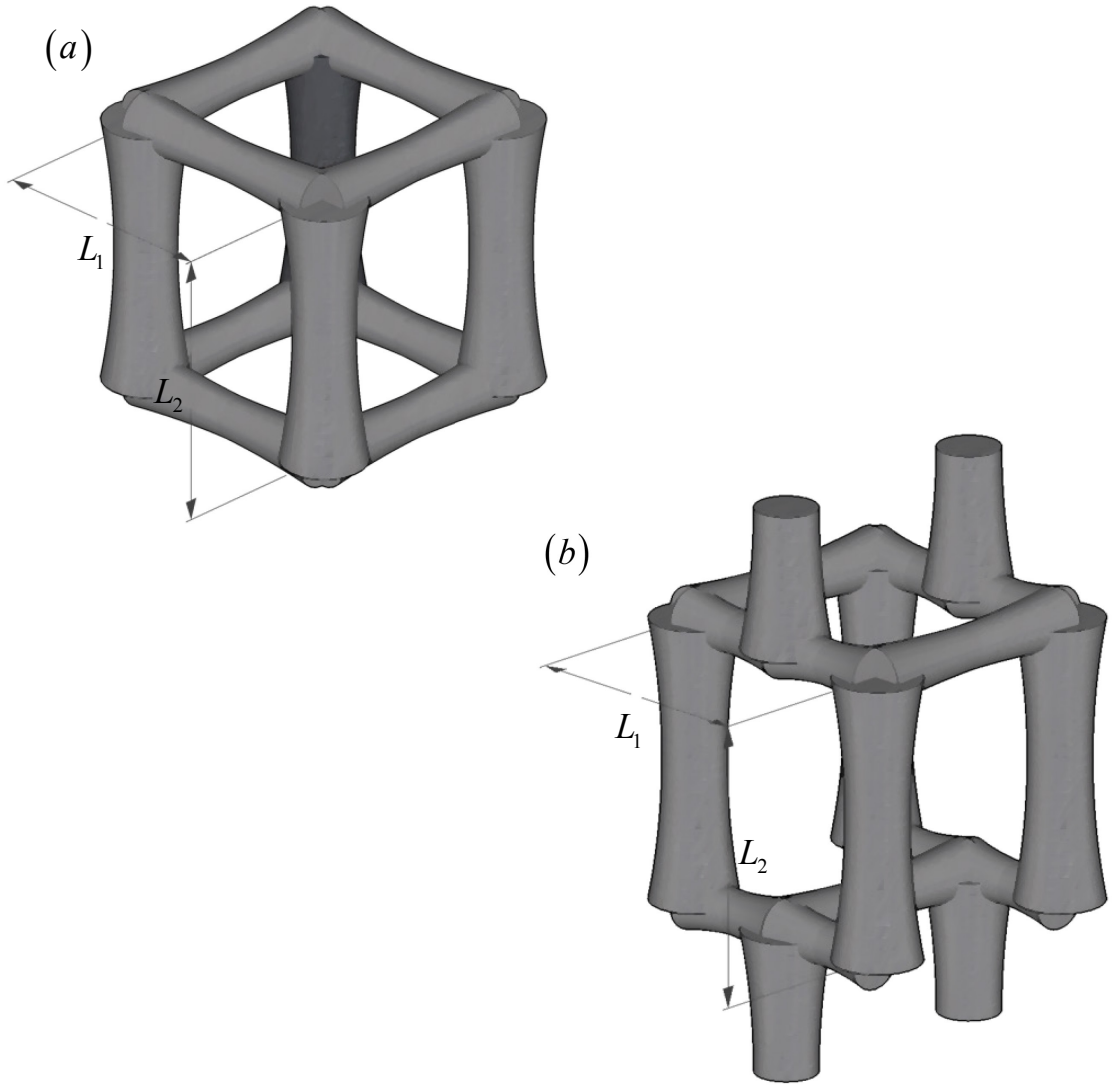

Figure 7-2. Representative idealized unit cells – (a) rectangular and (b) offset rectangular

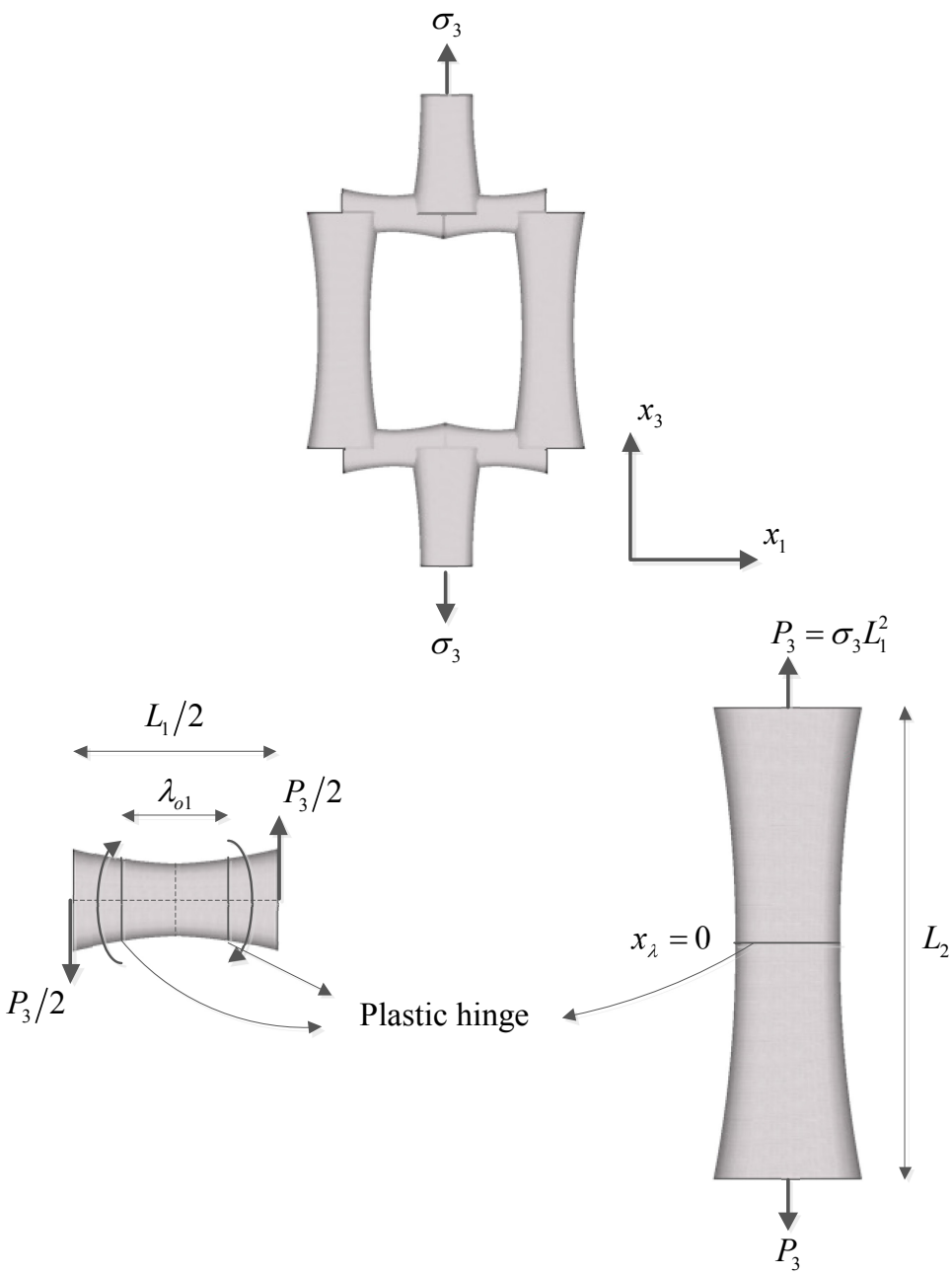

Figure 7-3. Forces, moments and plastic hinges imposed on the struts due to the stress σ_3 in the x_3 direction for the offset rectangular unit cell.

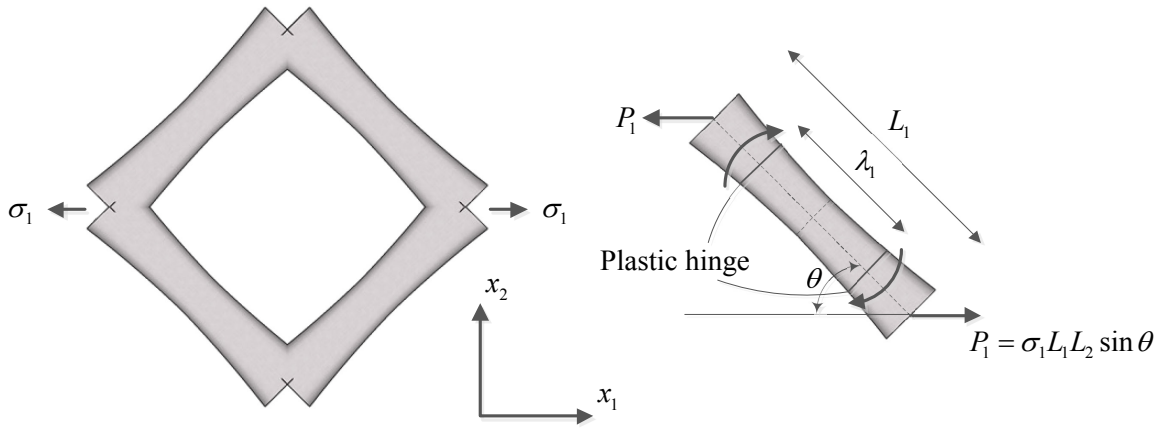

Figure 7-4. Forces, moments and plastic hinges imposed on the struts due to the stress σ_1 in the x_1 direction for the rectangular unit cell in the soft direction.

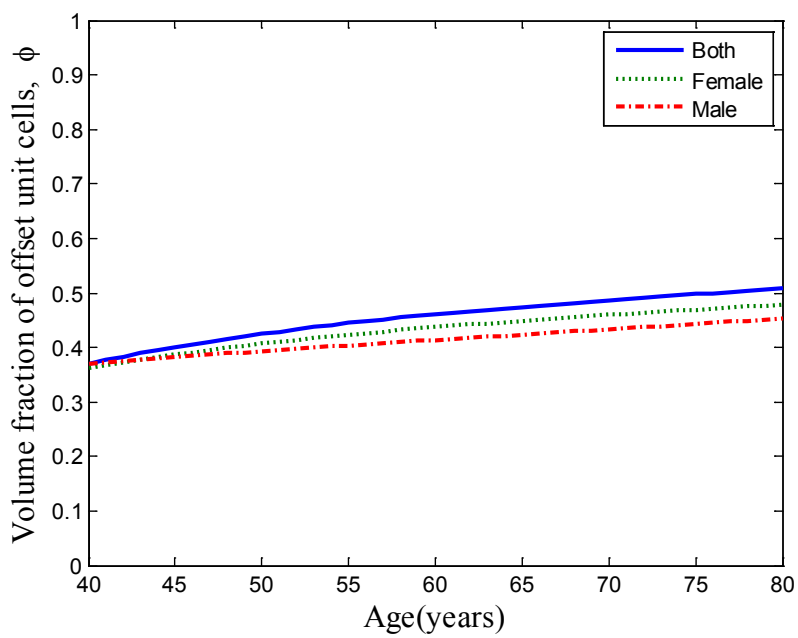

Figure 7-5. Volume fraction of offset unit cells as a function of age for the current model.

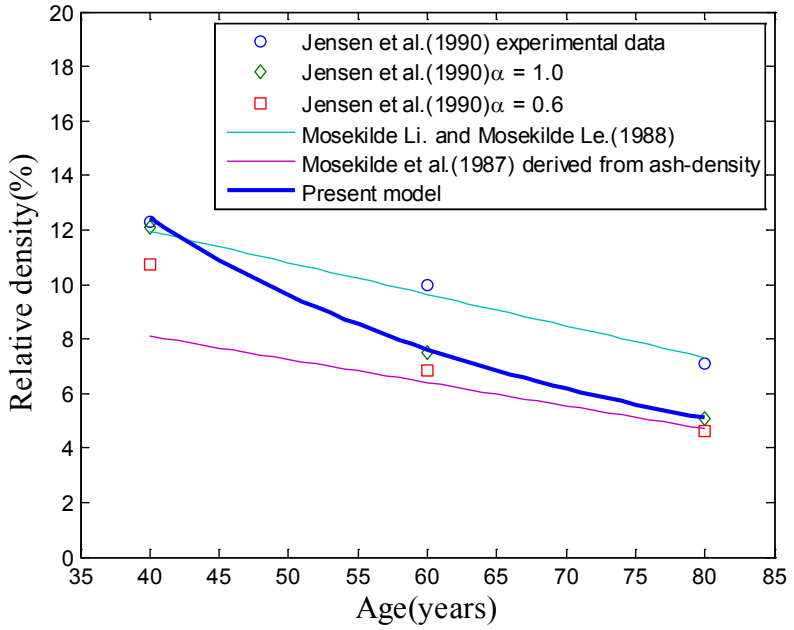

Figure 7-6. Relative density(%) of vertebral cancellous bone as a function of age.

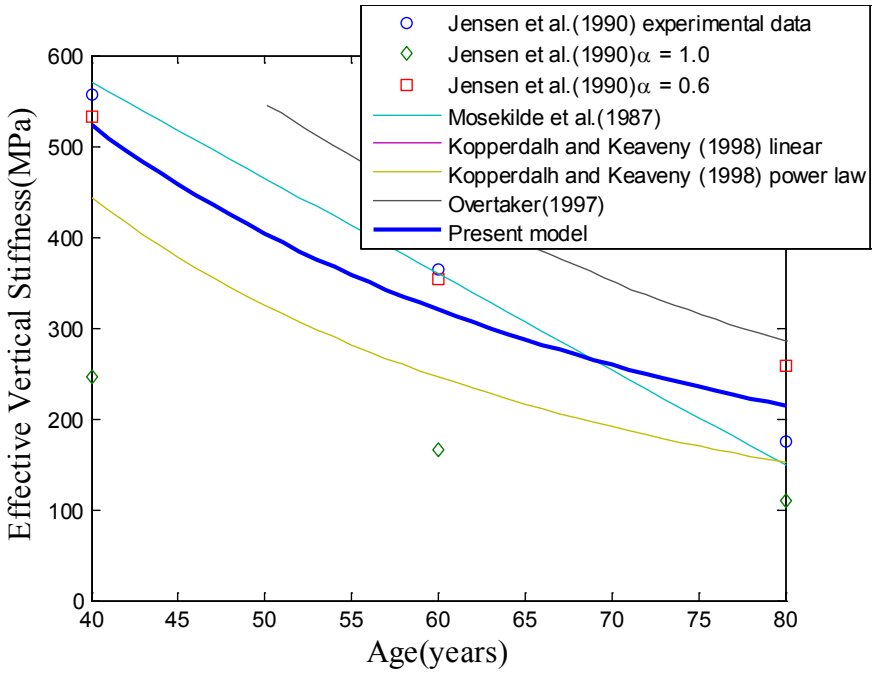

Figure 7-7. Effective vertical Young's modulus as a function of age.

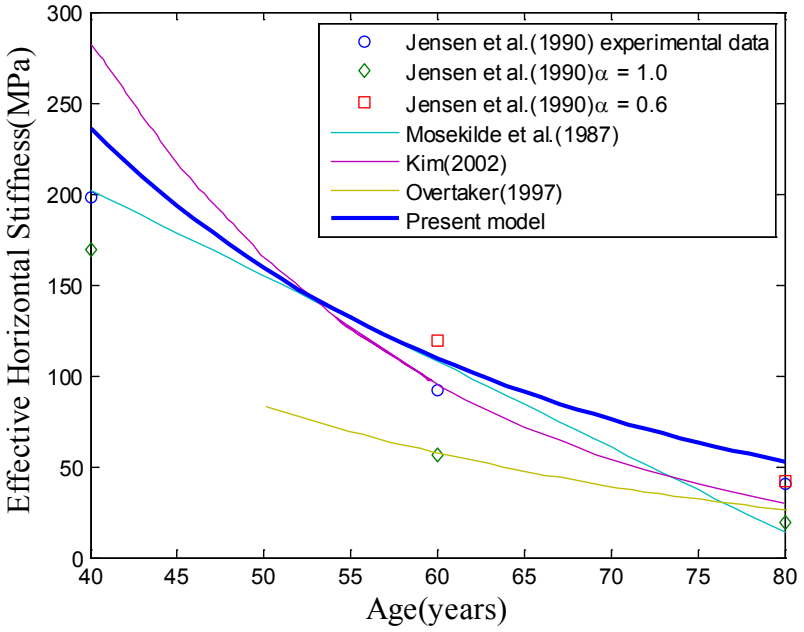

Figure 7-8. Effective horizontal Young's modulus as a function of age.

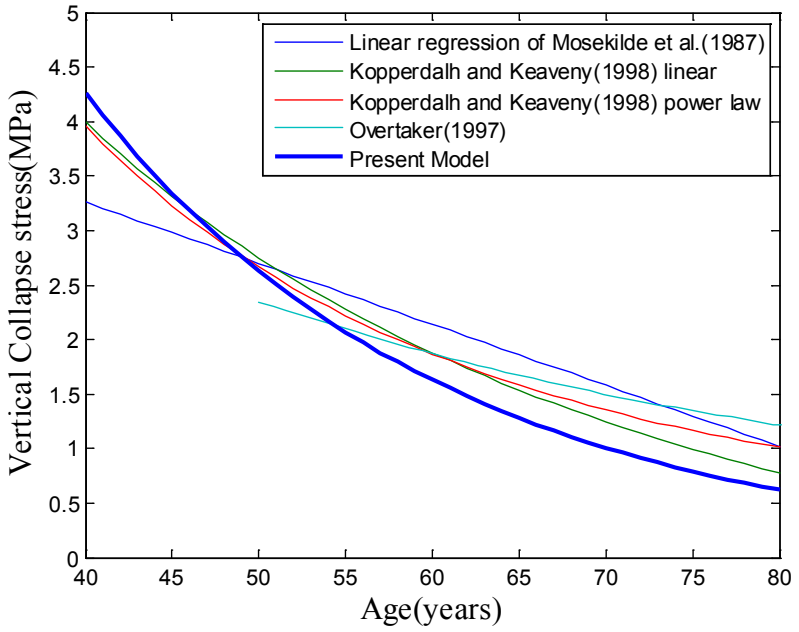

Figure 7-9. The vertical collapse stress as a function of age.

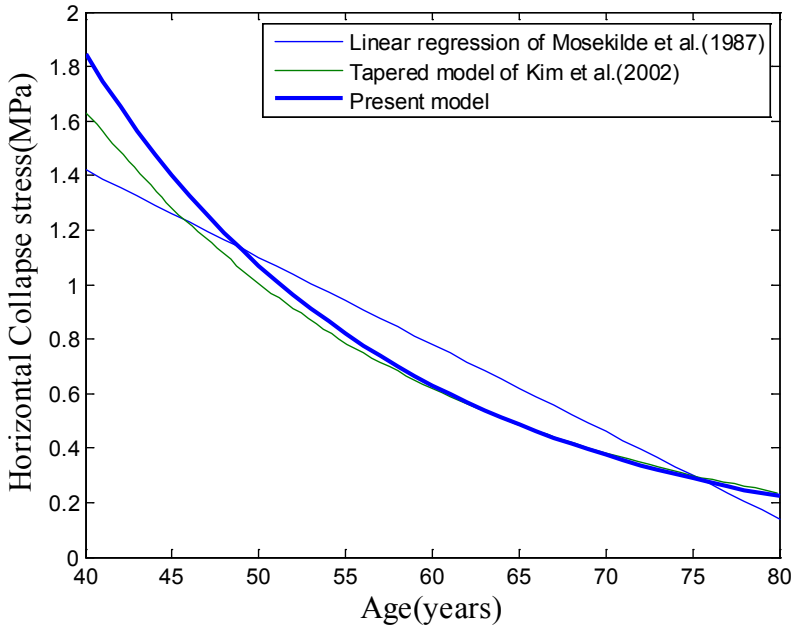

Figure 7-10. The horizontal collapse stress as a function of age.

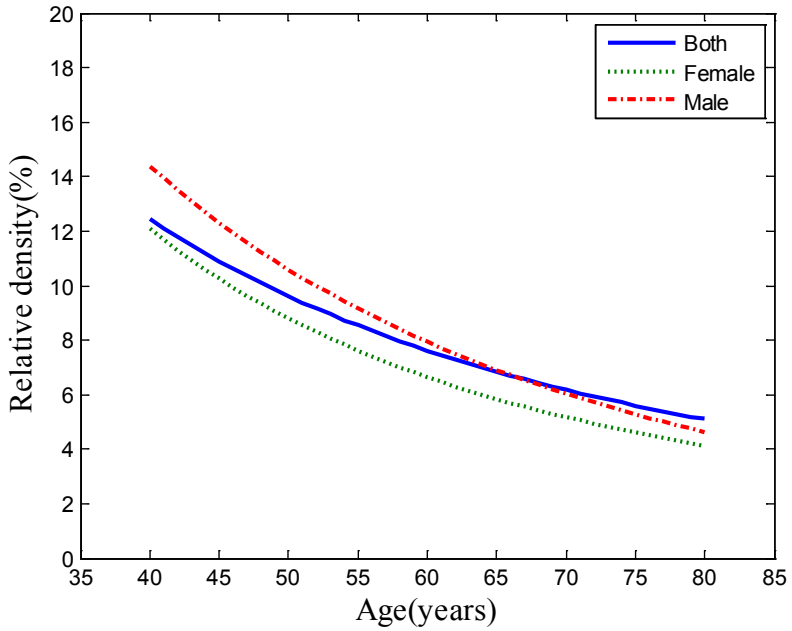

Figure 7-11. Sex-related differences in the relative density as a function of age.

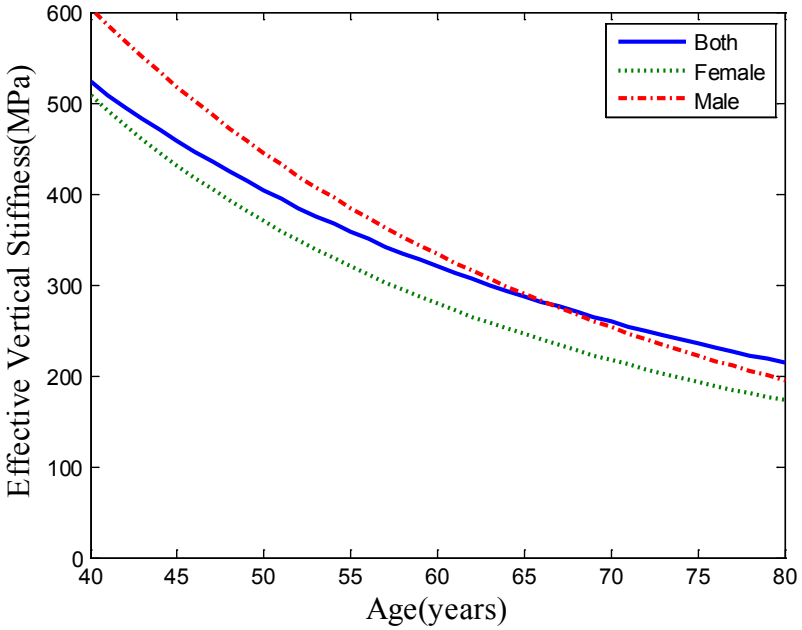

Figure 7-12. Sex-related differences in the effective vertical stiffness as a function of age.

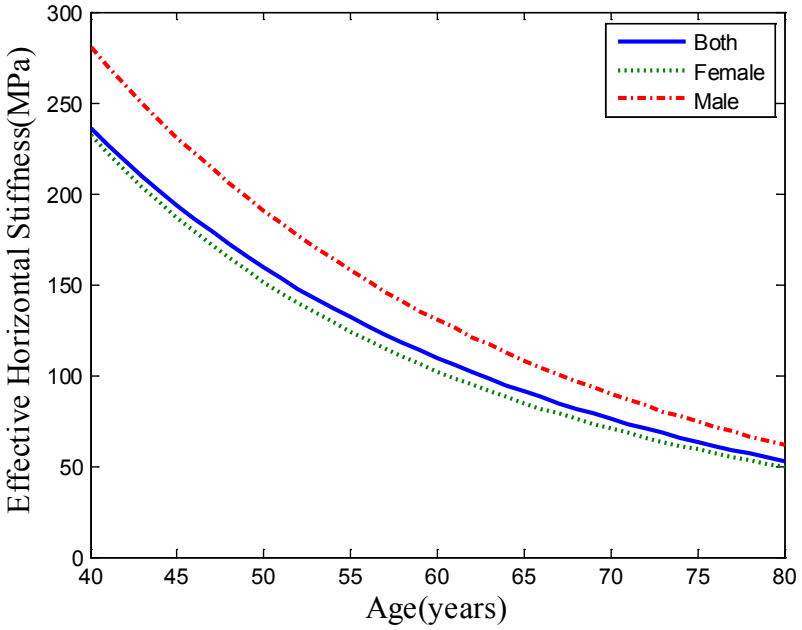

Figure 7-13. Sex-related differences in the effective horizontal stiffness as a function of age.

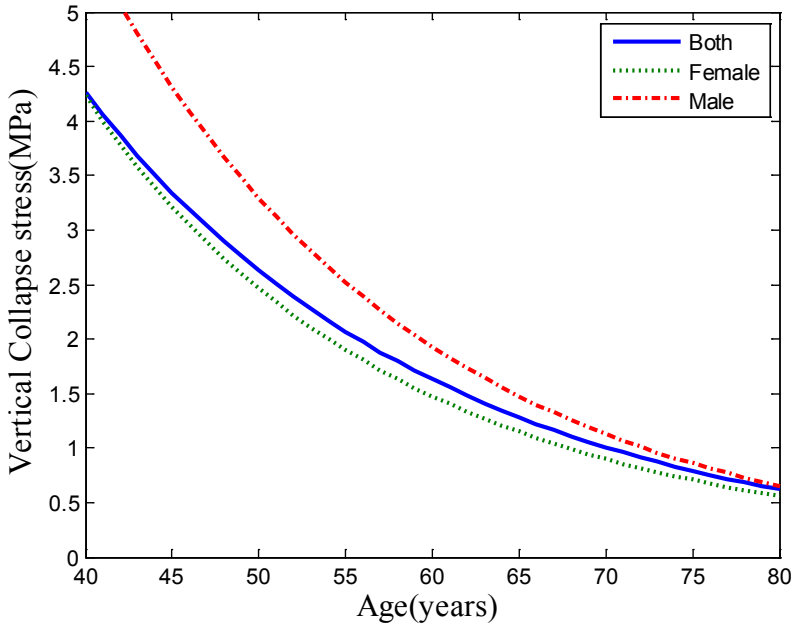

Figure 7-14. Sex-related differences in the vertical collapse stress as a function of age.

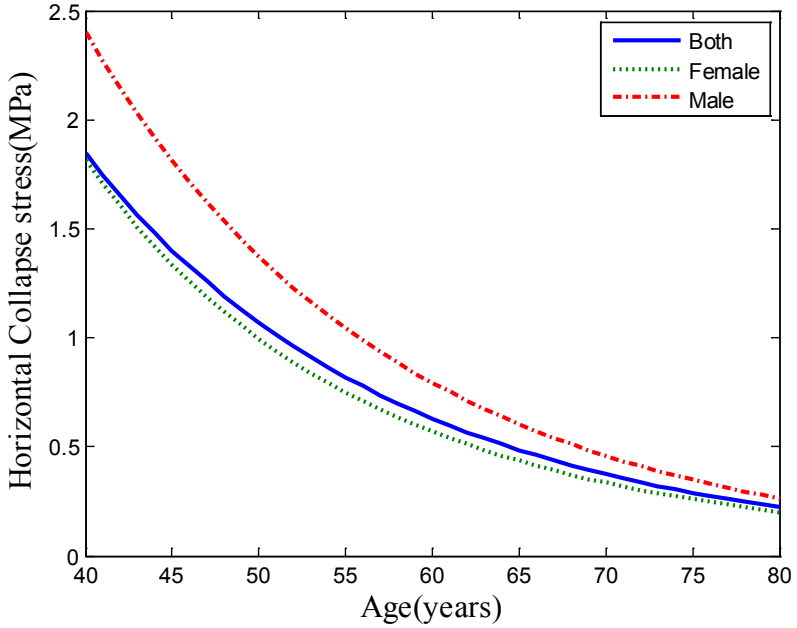

Figure 7-15. Sex-related differences in the horizontal collapse stress as a function of age.

7.6 Appendix VIII: Elastic Models of Rectangular Unit Cells

In this section, the effective stiffness for the rectangular and offset rectangular unit cells as shown in **Figure 7-2**, which have horizontal struts (of length L_1) and vertical struts (of length L_2) is derived. Due to the spatially periodic nature of unit cell structure, the individual struts deform anti-symmetrically about their mid-spans [50]. Consequently, there is no resultant moment across the strut section at the mid-span, and the mechanical properties for the unit cells can be approximately determined from those of cantilever beams.

The total strain energy U in a strut of length L due to a bending moment M, axial force R, and shear force V can be expressed as

$$U = \int_0^{L/2} \frac{M^2}{EI(x)} dx + \int_0^{L/2} \frac{R^2}{EA(x)} dx + \int_0^{L/2} \frac{kV^2}{GA(x)} dx \tag{7.23}$$

where E, G, and ν are Young's modulus, shear modulus, and Poisson's ratio of the material, k is a shear correction coefficient depending on the strut cross section, and $A(x)$ and $I(x)$ are the cross-sectional area and the second moment of the area associated with the cross section of the strut.

7.6.1 Effective Stiffness of Offset Rectangular Unit Cells

The remote stress σ_1 along the x_1 direction produces a force $P_1/2$ on the horizontal strut, as shown in **Figure 7-16**, resulting in a total strain energy stored in the unit cell as

$$U_1 = 4\int_0^{L_1/4} \frac{\left(P_1/2\right)^2}{EA_1\left(x\right)} dx = P_1^2 M_{o1} \tag{7.24}$$

The displacement δ_1 of the unit cell in the x_1 direction due to the force P_1 is obtained from Eq. (7.24)

$$\delta_1 = \frac{\partial U_1}{\partial P_1} = 2P_1 M_{o1} \tag{7.25}$$

The strain of the unit cell in the x_1 direction is given by

$$\varepsilon_1 = \frac{\delta_1}{L_1} = \frac{2P_1 M_{o1}}{L_1} \tag{7.26}$$

From **Figure 7-16**, we have $P_1 = 2\sigma_1 L_1 L_2$, and by this with combining Eq. (7.26), the effective Young's modulus parallel to x_1 is

$$E_{o1}^* = \frac{\sigma_1}{\varepsilon_1} = \frac{1}{4L_2 M_{o1}} \tag{7.27}$$

The stress σ_3 parallel to the x_3 produces an axial load P_3 on the vertical strut and transverse load $P_3/2$ on the horizontal strut as shown in **Figure 7-17**. For $V = P_3/2$ and $M\left(x\right) = Vx$, the strain energy in the horizontal struts is given by

$$\left(U_3\right)_1 = P_3^2\left[N_{o1} + 2k\left(1+\nu\right)M_{o1}\right] \tag{7.28}$$

and the strain energy in the vertical struts is given by

$$\left(U_3\right)_2 = 2P_3^2 M_2 \tag{7.29}$$

The total displacement δ_3 of the unit cell in the x_3 direction due to the force P_3 is obtained from Eq. (7.28) and (7.29),

$$\delta_3 = \frac{\partial U_3}{\partial P_3} = 2P_3\left[N_{o1} + 2k\left(1+\nu\right)M_{o1} + 2M_2\right] \tag{7.30}$$

The strain parallel to x_3 direction is

$$\varepsilon_3 = \frac{\delta_3}{2L_2} = \frac{P_3\left[N_{o1} + 2k\left(1+\nu\right)M_{o1} + 2M_2\right]}{L_2} \tag{7.31}$$

From **Figure 7-17**, we have $P_3 = \sigma_3 L_1^2$, and by combining this with Eq. (7.31), the effective Young's modulus parallel to x_3 is

$$E_{o3}^* = \frac{\sigma_3}{\varepsilon_3} = \frac{L_2}{L_1^2\left[N_{o1} + 2k\left(1+\nu\right)M_{o1} + 2M_2\right]} \tag{7.32}$$

The remote shear stress τ_{13} produces a force F_1 on the vertical strut, and $F_1/2$ and F_3 on the horizontal strut, as shown in **Figure 7-18**, where the force F_1 and F_2 are

$$\begin{aligned} F_1 &= \tau_{13}L_1^2 \\ F_3 &= \tau_{13}L_1L_2 \end{aligned} \tag{7.33}$$

The effective shear deformation includes three parts, which are (1) the bending and shear deformation of the vertical struts, (2) the rigid-body rotation of the vertical struts due to the bending and shear deformation of the horizontal struts, and (3) the axial deformation of the horizontal struts. For $V = F_1$, from Eq. (7.23), the bending and shear deformation of the vertical strut is

$$\delta_1 = 2\tau_{13}L_1^2\left[N_2 + 2k(1+\nu)M_2\right] \tag{7.34}$$

where

$$N_2 = \int_0^{L_2/2} \frac{x^2}{EI_2\left(x\right)}dx \tag{7.35}$$

For $R = F_1/2$ and $V = F_3$, from Eq. (7.23), the bending and shear deformation and axial deflection of the horizontal strut are

$$\delta_2 = 2\tau_{13} L_1 L_2 \left[N_{o1} + 2k\left(1+\nu\right) M_{o1} \right] \tag{7.36}$$

$$\delta_3 = \tau_{13} L_1^2 M_{o1} \tag{7.37}$$

Therefore, the rigid-body rotation of the vertical strut due to the bending and shear deformation of the horizontal strut is obtained by the following equation

$$\delta_2 \frac{L_2}{L_1/2} = 4\tau_{13} L_2^2 \left[N_{o1} + 2k\left(1+\nu\right) M_{o1} \right] \tag{7.38}$$

From Eq. (7.34), (7.37) and (7.38), the shear strain is given by

$$\gamma_{13} = \frac{2\tau_{13} L_1^2 \left[N_2 + 2k(1+\nu) M_2 \right] + 4\tau_{13} L_2^2 \left[N_{o1} + 2k\left(1+\nu\right) M_{o1} \right] + \tau_{13} L_1^2 M_{o1}}{L_2} \tag{7.39}$$

resulting in the shear modulus

$$G_{o13}^* = \frac{L_2}{2L_1^2 \left[N_2 + 2k(1+\nu) M_2 \right] + 4L_2^2 \left[N_{o1} + 2k\left(1+\nu\right) M_{o1} \right] + L_1^2 M_{o1}} \tag{7.40}$$

The remote stress σ_2 parallel to x_2 produces an axial force $P_2/2$ on the horizontal strut as shown in **Figure 7-19**. For $R = P_2/2$, from Eq. (7.23), the strain is

$$\varepsilon_2 = \frac{\delta_2}{L_1} = 2\sigma_2 L_2 M_1 \tag{7.41}$$

where

$$M_1 = \int_0^{L_1/2} \frac{1}{EA_1\left(x\right)} dx \tag{7.42}$$

Combining $P_2 = 2L_1L_2\sigma_2$ and Eq. (7.41), the effective Young's modulus parallel to x_2 is

$$E_{o2}^* = \frac{\sigma_2}{\varepsilon_2} = \frac{1}{2L_2M_1} \tag{7.43}$$

The remote shear stress τ_{12} produces a force $F_1/2$ in the x_1 direction on the horizontal struts perpendicular to x_1-x_3 plane, and a force $F_2/5$, which is derived by assuming top and bottom struts have the same transverse deformations in the x_2 direction and ignoring the shear term, in the x_2 direction on the top horizontal struts perpendicular to x_2-x_3 plane as shown in Figure 7-20. The forces F_1 and F_2 are written in terms of the remote shear stress τ_{12} as

$$F_1 = F_2 = 2\tau_{12}L_1L_2 \tag{7.44}$$

Upon the substitution of $V = F_1/2$, the deflection of the horizontal struts in the x_1 direction is obtained from Eq. (7.23)

$$\delta_1 = F_1\left[N_1 + 2k\left(1+\nu\right)M_1\right] \tag{7.45}$$

where

$$N_1 = \int_0^{L_1/2} \frac{x^2}{EI_1\left(x\right)}dx \tag{7.46}$$

For $V = F_2/5$, the deflection of the horizontal struts in the x_2 direction can also be obtained as

$$\delta_2 = F_2\left[\frac{2}{5}N_1 + \frac{4}{5}k\left(1+\nu\right)M_1\right] \tag{7.47}$$

From Eq. (7.45) and (7.47), the shear strain is obtained

$$\gamma_{12} = \frac{F_1\left[N_1 + 2k\left(1+\nu\right)M_1\right]_1 + F_2\left[\frac{2}{5}N_1 + \frac{4}{5}k\left(1+\nu\right)M_1\right]}{L_1} \tag{7.48}$$

resulting in the shear modulus

$$G_{o12}^* = \frac{1}{\frac{14}{5}L_2N_1 + \frac{28}{5}k\left(1+\nu\right)L_2M_1} \tag{7.49}$$

The shear stress τ_{23} produces a force $F_3/2$ in the x_3 direction on the horizontal struts, a force F_2 in the x_2 direction on the vertical struts and a force $F_2/2$ on the horizontal struts as shown in **Figure 7-21**. The forces F_2 and F_3 are written in terms of the remote shear stress τ_{23} as

$$\begin{aligned} F_2 &= \tau_{23}L_1^2 \\ F_3 &= 2\tau_{23}L_1L_2 \end{aligned} \tag{7.50}$$

For $V = F_3/2$, from Eq. (7.23), the bending and shear deformation of the horizontal strut in the x_3 direction is

$$\delta_3 = F_3\left[N_1 + 2k\left(1+\nu\right)M_1\right] \tag{7.51}$$

In a similar manner, the bending and shear deformation of the vertical and horizontal struts in the x_2 direction is

$$\delta_2 = F_2\left[2N_2 + 4k\left(1+\nu\right)M_2 + N_{o1} + 2k\left(1+\nu\right)M_{o1}\right] \tag{7.52}$$

From Eq. (7.50), (7.51) and (7.52), the shear strain is obtained as

$$\gamma_{23} = \frac{\delta_3}{L_1} + \frac{\delta_2}{L_2} \tag{7.53}$$

resulting in the shear modulus

$$G_{o23}^* = \frac{L_2}{2L_2^2\left[N_1 + 2k\left(1+\nu\right)M_1\right] + L_1^2\left[2N_2 + 4k\left(1+\nu\right)M_2 + N_{o1} + 2k\left(1+\nu\right)M_{o1}\right]} \tag{7.54}$$

The transverse strains due to the force in the x_3 direction are negligible compared with the strain parallel to the x_3 direction, and vice versa. Therefore, the Poisson's ratios are assumed

$$\nu_{13}^* \cong \nu_{31}^* \cong \nu_{23}^* \cong \nu_{32}^* \cong 0 \tag{7.55}$$

Furthermore, ν_{12}^* and ν_{21}^* are also assumed to be zero in this coordinate configuration.

From these effective elastic constants, the effective stiffness matrix is given by

$$\boldsymbol{C} = \begin{bmatrix} \frac{1-\nu_{23}\nu_{32}}{E_2E_3\Delta} & \frac{\nu_{21}+\nu_{31}\nu_{23}}{E_2E_3\Delta} & \frac{\nu_{31}+\nu_{21}\nu_{32}}{E_2E_3\Delta} & 0 & 0 & 0 \\ \frac{\nu_{12}+\nu_{13}\nu_{32}}{E_3E_1\Delta} & \frac{1-\nu_{31}\nu_{13}}{E_3E_1\Delta} & \frac{\nu_{32}+\nu_{31}\nu_{12}}{E_3E_1\Delta} & 0 & 0 & 0 \\ \frac{\nu_{31}+\nu_{12}\nu_{23}}{E_1E_2\Delta} & \frac{\nu_{23}+\nu_{13}\nu_{21}}{E_1E_2\Delta} & \frac{1-\nu_{12}\nu_{21}}{E_1E_2\Delta} & 0 & 0 & 0 \\ 0 & 0 & 0 & G_{23} & 0 & 0 \\ 0 & 0 & 0 & 0 & G_{31} & 0 \\ 0 & 0 & 0 & 0 & 0 & G_{12} \end{bmatrix} \tag{7.56}$$

where

$$\Delta = \frac{1-\nu_{12}\nu_{21}-\nu_{23}\nu_{32}-\nu_{31}\nu_{13}-2\nu_{12}\nu_{23}\nu_{31}}{E_1E_2E_3} \tag{7.57}$$

7.6.2 Effective Stiffness of Rectangular Unit Cells

The effective elastic constants of rectangular unit cells in the two soft directions are given in [61] and reorganized as

$$E_1^* = E_2^* = \frac{1}{L_2\left[N_1 + M_1 + 2k\left(1+\nu\right)M_1\right]} \tag{7.58}$$

$$\nu_{12}^* = \nu_{21}^* = \frac{N_1 - M_1 + 2k\left(1+\nu\right)M_1}{N_1 + M_1 + 2k\left(1+\nu\right)M_1} \tag{7.59}$$

$$G_{12}^* = \frac{1}{4L_2M_1} \tag{7.60}$$

$$E_3^* = \frac{L_2}{2L_1^2M_2} \tag{7.61}$$

$$\nu_{13}^* \cong \nu_{23}^* \cong \nu_{31}^* \cong \nu_{32}^* \cong 0 \tag{7.62}$$

$$G_{13}^* = G_{23}^* = \frac{L_2}{2\left\{L_2^2\left[N_1 + 2k\left(1+\nu\right)M_1\right] + L_1^2\left[N_2 + 2k\left(1+\nu\right)M_2\right]\right\}} \tag{7.63}$$

7.7 Appendix IX: Transformation of Elastic Constants

Consider two orthogonal coordinate systems, (x_1, x_2, x_3) and (x_1', x_2', x_3'), where one is rotated about their common origin with respect to the other. The relationship between these two systems is

$$\begin{Bmatrix} x_1' \\ x_2' \\ x_3' \end{Bmatrix} = \begin{bmatrix} l_1 & m_1 & n_1 \\ l_2 & m_2 & n_2 \\ l_3 & m_3 & n_3 \end{bmatrix} \begin{Bmatrix} x_1 \\ x_2 \\ x_3 \end{Bmatrix} \tag{7.64}$$

The transformation of the stiffness matrix $\boldsymbol{C}$ can be expressed as

$$\boldsymbol{C}' = \boldsymbol{T}_1^T \boldsymbol{C} \boldsymbol{T}_1 \tag{7.65}$$

where $\boldsymbol{T}_1$ is a 6×6 transformation matrix given by

$$\boldsymbol{T}_1 = \begin{bmatrix} l_1^2 & m_1^2 & n_1^2 & 2m_1n_1 & 2l_1n_1 & 2l_1m_1 \\ l_2^2 & m_2^2 & n_2^2 & 2m_2n_2 & 2l_2n_2 & 2l_2m_2 \\ l_3^2 & m_3^2 & n_3^2 & 2m_3n_3 & 2l_3n_3 & 2l_3m_3 \\ l_2l_3 & m_2m_3 & n_2n_3 & m_2n_3 + m_3n_2 & l_2n_3 + l_3n_2 & l_2m_3 + l_3m_2 \\ l_1l_3 & m_1m_3 & n_1n_3 & m_1n_3 + m_3n_1 & l_1n_3 + l_3n_1 & l_1m_3 + l_3m_1 \\ l_1l_2 & m_1m_2 & n_1n_2 & m_1n_2 + m_2n_1 & l_1n_2 + l_2n_1 & l_1m_2 + l_2m_1 \end{bmatrix} \tag{7.66}$$

7.8 Appendix X: Criterion for Elastic Collapse and Plastic Collapse

The critical buckling stress (σ_{cr}) of an individual trabecula can be described by the Euler buckling equation:

$$\sigma_{cr} = \frac{\pi^2 E}{\left(4k\frac{L}{D}\right)^2} \tag{7.67}$$

where k is a constant of approximately 0.5 for a column with fixed ends. For failure to occur by buckling, the critical buckling stress (σ_{cr}) must be less than the compressive strength of the trabecula (σ_y). Therefore, the minimum slenderness ratio for buckling can be estimated by using the following equation:

$$\frac{L}{D} > \sqrt{\frac{\pi^2 E}{(4k)^2 \sigma_y}} \tag{7.68}$$

The minimum slenderness ratio for buckling can be estimated by substituting the modulus (E) and strength (σ_y) of the trabecular into Eq. (7.68), which have a value of 12GPa and 193MPa, respectively. Therefore, if the slenderness ratio is greater than 12.39, the trabeculae will buckle. In this study, both slenderness ratios of horizontal and vertical trabeculae are smaller than 9.3, thus the plastic collapse dominates.

Gibson and Ashby [54] also present a criterion for open-cell foams to evaluate if it is possible for elastic collapse to precede plastic collapse as

$$\rho^* < 36\left(\frac{\sigma_y}{E}\right)^2 \tag{7.69}$$

Upon substituting σ_y and E into Eq. (7.69), elastic collapse precedes plastic collapse when the relative density is below 0.0093. As shown in **Figure 7-6**, the relative densities in this study are all above 0.0093 and therefore the plastic collapse controls.

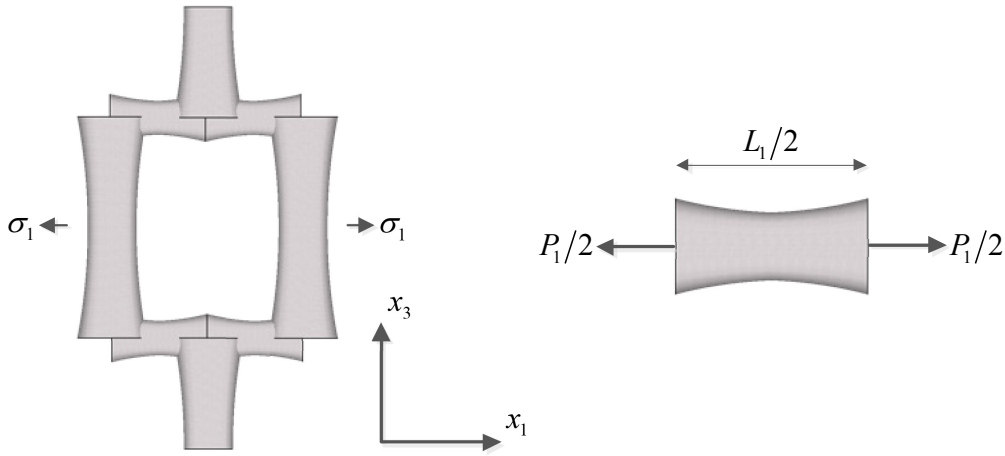

Figure 7-16. Free-body diagram of the struts due to the stress σ_1 in the x_1 direction

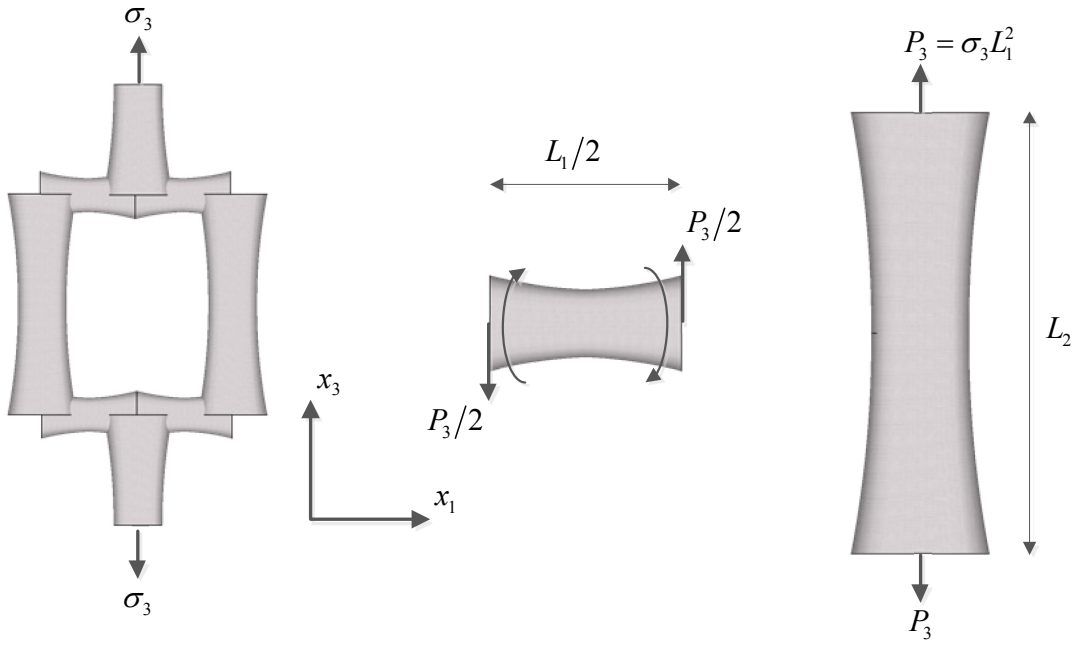

Figure 7-17. Free-body diagram of the struts due to the stress σ_3 in the x_3 direction

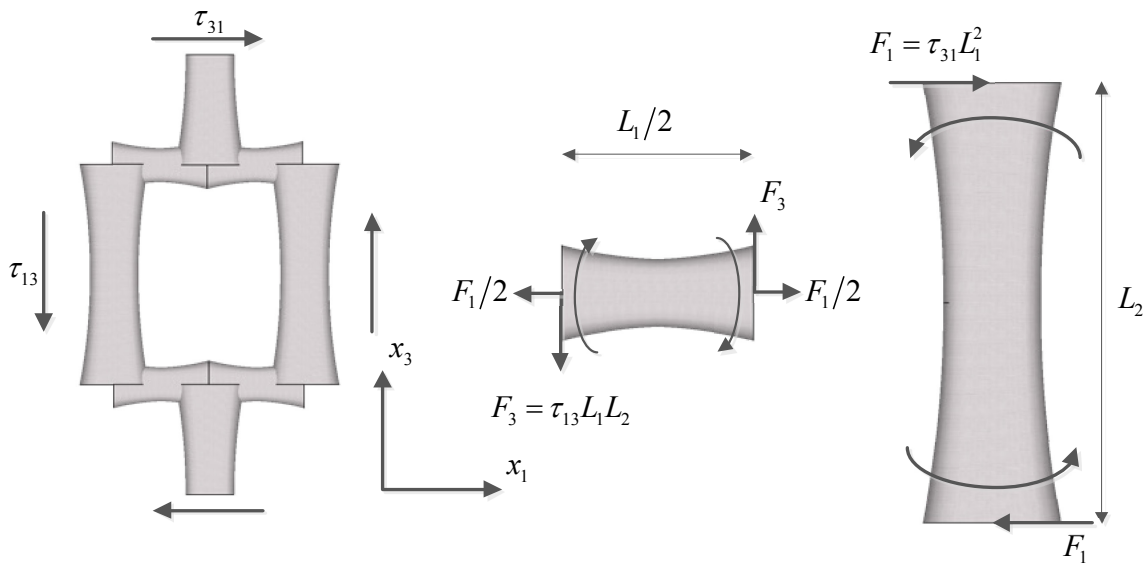

Figure 7-18. Free-body diagram of the struts due to the shear stress τ_{13}

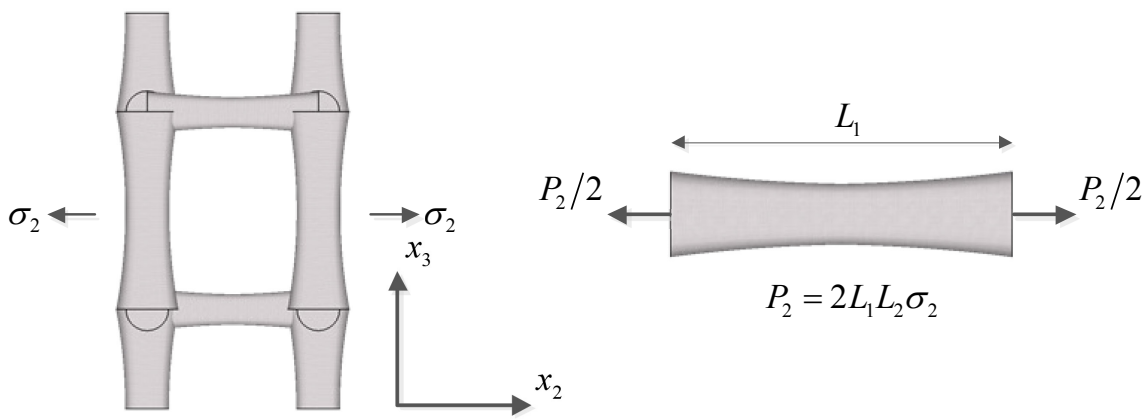

Figure 7-19. Free-body diagram of the struts due to the stress σ_2 in the x_2 direction

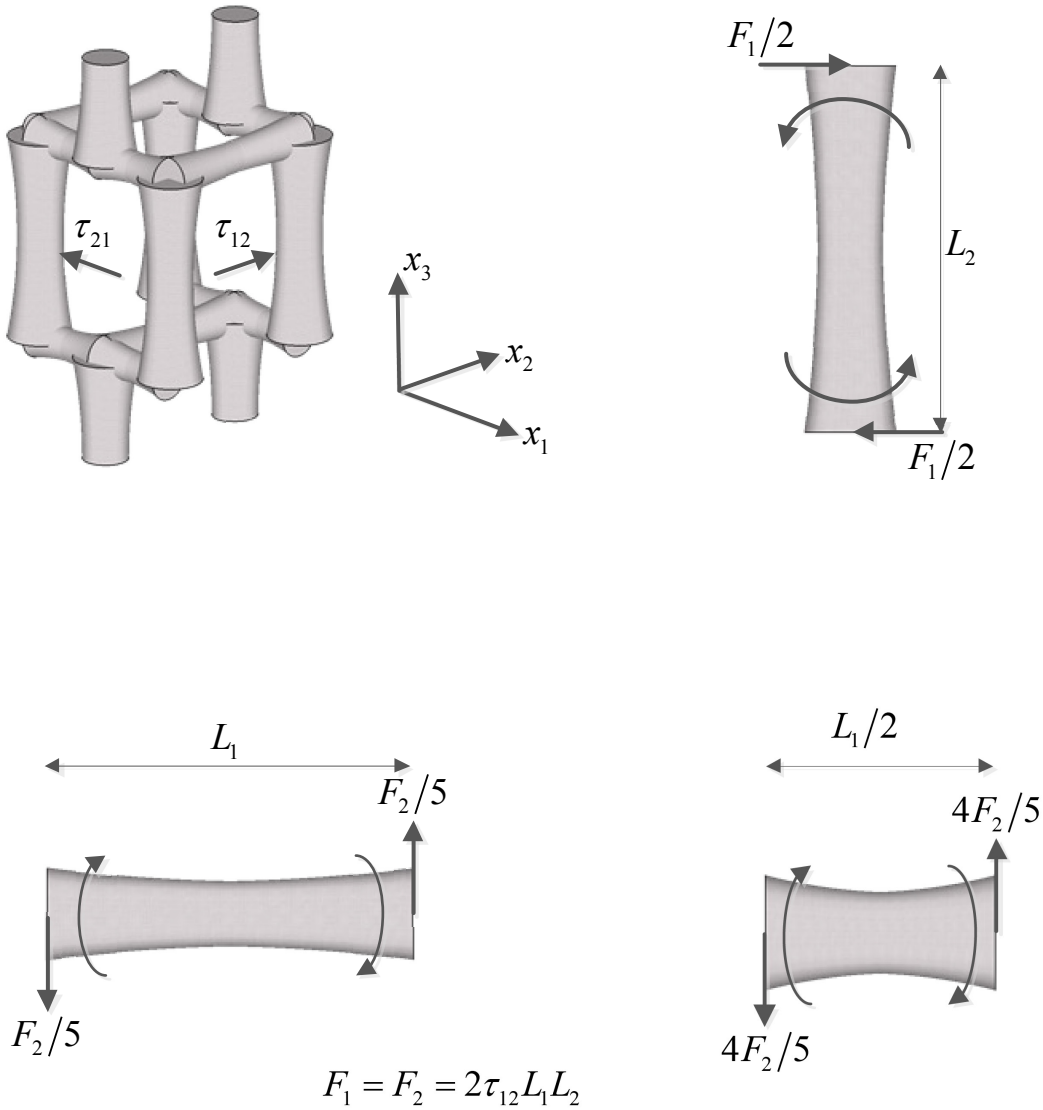

Figure 7-20. Free-body diagram of the struts due to the shear stress τ_{12}

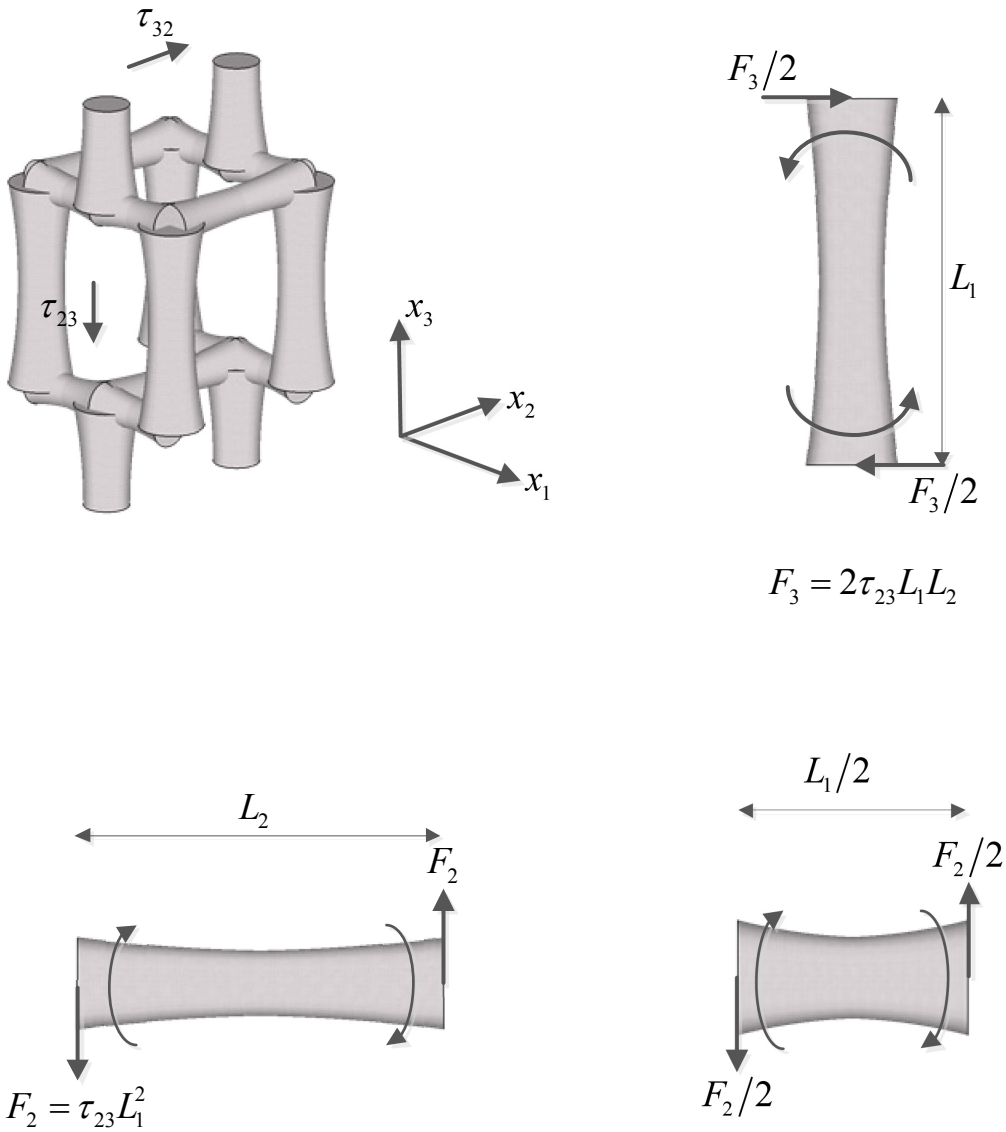

Figure 7-21. Free-body diagram of the struts due to the shear stress τ_{23}

7.9 References

1. Riggs, B.L. and L.J. Melton, *The worldwide problem of osteoporosis: Insights afforded by epidemiology.* Bone, 1995. **17**(5, Supplement 1): p. S505-S511.
2. Obrant, K., et al., *Increasing age-adjusted risk of fragility fractures: A sign of increasing osteoporosis in successive generations?* Calcified Tissue International, 1989. **44**(3): p. 157-167.
3. Mosekilde, L., *Vertebral structure and strength In vivo and In vitro.* Calcified Tissue International, 1993. **53**(0): p. S121-S126.
4. Mosekilde, L., *Age-related changes in vertebral trabecular bone architecture--assessed by a new method.* Bone, 1988. **9**(4): p. 247-50.
5. Mosekilde, L., *Sex differences in age-related loss of vertebral trabecular bone mass and structure--biomechanical consequences.* Bone, 1989. **10**(6): p. 425-432.
6. Whitehouse, W.J., E.D. Dyson, and C.K. Jackson, *The scanning electron microscope in studies of trabecular bone from a human vertebral body.* J Anat, 1971. **108**(Pt 3): p. 481-96.
7. Goldstein, S.A., R. Goulet, and D. McCubbrey, *Measurement and significance of three-dimensional architecture to the mechanical integrity of trabecular bone.* Calcified Tissue International, 1993. **53**(0): p. S127-S133.
8. Atkinson, P.J., *Variation in trabecular structure of vertebrae with age.* Calcif Tissue Res, 1967. **1**(1): p. 24-32.
9. Bell, G.H., et al., *Variations in strength of vertebrae with age and their relation to osteoporosis.* Calcif Tissue Res, 1967. **1**(1): p. 75-86.

10. Vesterby, A., et al., *Biologically meaningful determinants of the in vitro strength of lumbar vertebrae.* Bone, 1991. **12**(3): p. 219-24.

11. Snyder, B.D., et al., *Role of trabecular morphology in the etiology of age-related vertebral fractures.* Calcified Tissue International, 1993. **53**(0): p. S14-S22.

12. Vogel, M., M. Hahn, and G. Delling, *Relation between 2- and 3-dimensional architecture of trabecular bone in the human spine.* Bone. **14**(3): p. 199-203.

13. Pugh, J.W., R.M. Rose, and E.L. Radin, *A structural model for the mechanical behavior of trabecular bone.* Journal of Biomechanics, 1973. **6**(6): p. 657-670.

14. Williams, J.L. and J.L. Lewis, *Properties and an anisotropic model of cancellous bone from the proximal tibial epiphysis.* J Biomech Eng, 1982. **104**(1): p. 50-6.

15. Beaupre, G.S. and W.C. Hayes, *Finite element analysis of a three-dimensional open-celled model for trabecular bone.* J Biomech Eng, 1985. **107**(3): p. 249-56.

16. Gibson, L.J., *The mechanical behaviour of cancellous bone.* Journal of Biomechanics, 1985. **18**(5): p. 317-328.

17. Jensen, K.S., L. Mosekilde, and L. Mosekilde, *A model of vertebral trabecular bone architecture and its mechanical properties.* Bone, 1990. **11**(6): p. 417-423.

18. Hollister, S.J., et al., *Application of homogenization theory to the study of trabecular bone mechanics.* J Biomech, 1991. **24**(9): p. 825-39.

19. Overaker, D.W., *Micromechanical modeling of open cell structures with application in finite element analysis of vertebral body mechanics*, in *Mechanical and Aerospace Engineering*1997, Rutgers, The state University of New Jersey: New Jersey.

20. Kim, H.S. and S.T.S. Al-Hassani, *A morphological model of vertebral trabecular bone.* Journal of Biomechanics, 2002. **35**(8): p. 1101-1114.

21. Sander, E.A., et al., *Examination of continuum and micro-structural properties of human vertebral cancellous bone using combined cellular solid models.* Biomech Model Mechanobiol, 2003. **2**(2): p. 97-107.

22. van Rietbergen, B., et al., *A new method to determine trabecular bone elastic properties and loading using micromechanical finite-element models.* J Biomech, 1995. **28**(1): p. 69-81.

23. Hou, F.J., et al., *Human vertebral body apparent and hard tissue stiffness.* Journal of Biomechanics, 1998. **31**(11): p. 1009-1015.

24. Ladd, A.J., et al., *Finite-element modeling of trabecular bone: comparison with mechanical testing and determination of tissue modulus.* J Orthop Res, 1998. **16**(5): p. 622-8.

25. Kabel, J., et al., *The role of an effective isotropic tissue modulus in the elastic properties of cancellous bone.* J Biomech, 1999. **32**(7): p. 673-80.

26. Niebur, G.L., et al., *Convergence behavior of high-resolution finite element models of trabecular bone.* J Biomech Eng, 1999. **121**(6): p. 629-35.

27. Niebur, G.L., et al., *High-resolution finite element models with tissue strength asymmetry accurately predict failure of trabecular bone.* J Biomech, 2000. **33**(12): p. 1575-83.

28. Homminga, J., et al., *Introduction and evaluation of a gray-value voxel conversion technique.* J Biomech, 2001. **34**(4): p. 513-7.

29. Verhulp, E., et al., *Micro-finite element simulation of trabecular-bone post-yield behaviour – effects of material model, element size and type.* Comput Methods Biomech Biomed Engin, 2008. **11**(4): p. 389 - 395.

30. Thomsen, J.S., E.N. Ebbesen, and L. Mosekilde, *Zone-dependent changes in human vertebral trabecular bone: Clinical implications.* Bone, 2002. **30**(5): p. 664-669.

31. Ryan, S.D. and J.L. Williams, *Tensile testing of rodlike trabeculae excised from bovine femoral bone.* Journal of Biomechanics, 1989. **22**(4): p. 351-355.

32. Rho, J.Y., R.B. Ashman, and C.H. Turner, *Young's modulus of trabecular and cortical bone material: Ultrasonic and microtensile measurements.* Journal of Biomechanics, 1993. **26**(2): p. 111-119.

33. Runkle, J.C. and J. Pugh, *The micro-mechanics of cancellous bone. II. Determination of the elastic modulus of individual trabeculae by a buckling analysis.* Bull Hosp Joint Dis, 1975. **36**(1): p. 2-10.

34. Townsend, P.R., R.M. Rose, and E.L. Radin, *Buckling studies of single human trabeculae.* Journal of Biomechanics, 1975. **8**(3-4): p. 199-200, IN5-IN6, 201.

35. Kuhn, J.L., et al., *The mechanical properties of single trabecula.* Trans. 33rd Orthopaedics Research Society, 1987. **I**: p. 48.

36. Choi, K., et al., *The elastic moduli of human subchondral, trabecular, and cortical bone tissue and the size-dependency of cortical bone modulus.* J Biomech, 1990. **23**(11): p. 1103-13.

37. Kuhn, J.L., et al., *Comparison of the trabecular and cortical tissue moduli from human iliac crests.* Journal of Orthopaedic Research, 1989. **7**(6): p. 876-884.

38. Mente, P.L. and J.L. Lewis, *Young's modulus of trabecular bone tissue.* Trans. 33rd Orthopaedics Research Society, 1987. **12**: p. 49.

39. Mente, P.L. and J.L. Lewis, *Experimental method for the measurement of the elastic modulus of trabecular bone tissue.* Journal of Orthopaedic Research, 1989. **7**(3): p. 456-461.

40. Ashman, R.B. and J.Y. Rho, *Elastic modulus of trabecular bone material.* J Biomech, 1988. **21**(3): p. 177-81.

41. Silva, M.J. and L.J. Gibson, *Modeling the mechanical behavior of vertebral trabecular bone: Effects of age-related changes in microstructure.* Bone, 1997. **21**(2): p. 191-199.

42. Gibson, L.J. and M.F. Ashby, *Cellular Solids: Structure and properties*. 2nd ed1997, Cambridge: Cambridge University Press.

43. Reilly, D.T. and A.H. Burstein, *The elastic and ultimate properties of compact bone tissue.* Journal of Biomechanics, 1975. **8**(6): p. 393-396, IN9-IN11, 397-405.

44. Currey, J.D., *The mechanical adaptations of bones*1984, Princeton, N.J.: Princeton University Press.

45. Fritsch, A. and C. Hellmich, *`Universal' microstructural patterns in cortical and trabecular, extracellular and extravascular bone materials: Micromechanics-based prediction of anisotropic elasticity.* Journal of Theoretical Biology, 2007. **244**(4): p. 597-620.

46. Turner, C.H., et al., *The elastic properties of trabecular and cortical bone tissues are similar: results from two microscopic measurement techniques.* Journal of Biomechanics, 1999. **32**(4): p. 437-441.

47. Christensen, R.M., *Mechanics of cellular and other low-density materials.* International Journal of Solids and Structures, 2000. **37**(1-2): p. 93-104.

48. Kopperdahl, D.L. and T.M. Keaveny, *Yield strain behavior of trabecular bone.* J Biomech, 1998. **31**(7): p. 601-8.

49. Lees, S., *Considerations regarding the structure of the mammalian mineralized osteoid from viewpoint of the generalized packing model.* Connect Tissue Res, 1987. **16**(4): p. 281-303.

50. Kim, H.S. and S.T.S. Al-Hassani, *Plastic collapse of cellular structures comprised of doubly tapered struts.* International Journal of Mechanical Sciences, 2001. **43**(11): p. 2453-2478.

51. Stronge, W.J. and T.X. Yu, *Dynamic models for structural plasticity*1993, London; New York: Springer-Verlag.

52. Gibson, L.J., *Cellular solids : structure & properties / Lorna J. Gibson, Michael F. Ashby*, ed. M.F. Ashby1988, Oxford [Oxfordshire] ; New York :: Pergamon Press.

53. Gibson, L.J., et al., *Failure surfaces for cellular materials under multiaxial loads--I.Modelling.* International Journal of Mechanical Sciences, 1989. **31**(9): p. 635-663.

54. Gibson, L.J. and M.F. Ashby, *Cellular solids : structure and properties*. Cambridge solid state science series1997, Cambridge; New York: Cambridge University Press.

55. Mosekilde, L. and L. Mosekilde, *Sex differences in age-related changes in vertebral body size, density and biomechanical competence in normal individuals.* Bone, 1990. **11**(2): p. 67-73.

56. Mosekilde, L., L. Mosekilde, and C.C. Danielsen, *Biomechanical competence of vertebral trabecular bone in relation to ash density and age in normal individuals.* Bone, 1987. **8**(2): p. 79-85.

57. Hildebrand, T. and P. Ruegsigger, *Quantification of Bone Microarchitecture with the Structure Model Index.* Comput Methods Biomech Biomed Engin, 1997. **1**(1): p. 15 - 23.

58. Choi, K. and S.A. Goldstein, *The fatigue properties of bone tissues on a microstructural level.* Transaction of the Orthopaedics Research Society, 1991. **16**: p. 485.

59. Van Rietbergen, B., et al., *Trabecular bone tissue strains in the healthy and osteoporotic human femur.* J Bone Miner Res, 2003. **18**(10): p. 1781-8.

60. Bini, F., et al., *Microtensile measurements of single trabeculae stiffness in human femur.* Journal of Biomechanics, 2002. **35**(11): p. 1515-1519.

61. Kim, H.S. and S.T.S. Al-Hassani, *A morphological elastic model of general hexagonal columnar structures.* International Journal of Mechanical Sciences, 2001. **43**(4): p. 1027-1060.